eScience 4 (2024) 100222

Contents lists available at ScienceDirect

eScience

journal homepage: www.keaipublishing.com/en/journals/escience

Research Paper

Understanding synergistic catalysis on Pt–Cu diatomic sites via *operando* X-ray absorption spectroscopy in sulfur redox reactions

Shuai Xie [a,1], Xingjia Chen [b,1], Leilei Wang [c,1], Guikai Zhang [d], Haifeng Lv [b], Guolei Cai [a], Ying-Rui Lu [e], Ting-Shan Chan [e], Jing Zhang [d], Juncai Dong [d], Hongchang Jin [a], Xianghua Kong [f], Junling Lu [c], Song Jin [a,*], Xiaojun Wu [b,*], Hengxing Ji [a,*]

[a] *Hefei National Laboratory for Physical Sciences at the Microscale, CAS Key Laboratory of Materials for Energy Conversion, Department of Applied Chemistry, University of Science and Technology of China, Hefei 230026, China*
[b] *School of Chemistry and Material Sciences, CAS Key Laboratory of Materials for Energy Conversion, and CAS Center for Excellence in Nanoscience and Synergetic Innovation of Quantum Information and Quantum Technology, University of Science and Technology of China, Hefei 230026, China*
[c] *Hefei National Laboratory for Physical Sciences at the Microscale, Department of Chemical Physics, School of Chemistry and Materials Science, University of Science and Technology of China, Hefei 230026, China*
[d] *Beijing Synchrotron Radiation Laboratory, Institute of High Energy Physics, Chinese Academy of Sciences, Beijing 100049, China*
[e] *National Synchrotron Radiation Research Center, Hsinchu 300092, China*
[f] *School of Chemistry and Chemical Engineering, Hefei University of Technology, Hefei 230009, China*

HIGHLIGHTS

- Pt–Cu dual-atomic sites boost sulfur redox reaction kinetics for Li–S batteries.
- *Operando* X-ray absorption spectroscopy (XAS) reveals the synergistic effects operative in Dual-atom catalysts on the atomic scale.
- A synergistic effect between Pt and Cu atoms modifies the electronic structure of the Pt site through d-orbital interactions.

GRAPHICAL ABSTRACT

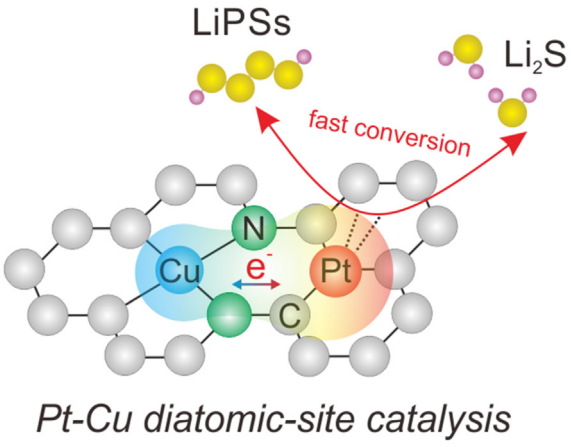

ARTICLE INFO

Keywords:
Dual-atom catalysts
Sulfur redox reaction
Lithium–sulfur batteries
Synergistic interaction
X-ray absorption spectroscopy

ABSTRACT

Sulfur redox reactions render lithium–sulfur (Li–S) batteries with an energy density of > 500 Wh kg^{-1} but suffer a low practical capacity and fast capacity fade due to sluggish sulfur redox reaction (SRR) kinetics, which lies in the complex reaction process that involves a series of reaction intermediates and proceeds via a cascade reaction. Here, we present a Pt–Cu dual-atom catalyst (Pt/Cu-NG) as an electrocatalyst for sulfur redox reactions. Pt/Cu-NG enabled the rapid conversion of soluble polysulfide intermediates into insoluble Li_2S_2/Li_2S, and consequently, it

* Corresponding authors.
E-mail addresses: js199155@ustc.edu.cn (S. Jin), xjwu@ustc.edu.cn (X. Wu), jihengx@ustc.edu.cn (H. Ji).
[1] These authors contributed equally.

https://doi.org/10.1016/j.esci.2023.100222
Received 19 October 2023; Received in revised form 23 November 2023; Accepted 29 November 2023
Available online 13 December 2023

prevented the accumulation and shuttling of lithium polysulfides, thus outperforming the corresponding single-atom catalysts (SACs) with individual Pt or Cu sites. *Operando* X-ray absorption spectroscopy and density functional theory calculations revealed that a synergistic effect between the paired Pt and Cu atoms modifies the electronic structure of the Pt site through d-orbital interactions, resulting in an optimal moderate interaction of the metal atom with the different sulfide species. This optimal interaction enhanced charge transfer kinetics and promoted sulfur redox reactions. Our work thus provides important insights on the atomic scale into the synergistic effects operative in dual-atom catalysts and will thus pave the way to electrocatalysts with enhanced efficiency for high-performance Li–S batteries.

1. Introduction

Lithium–sulfur (Li–S) batteries hold great promise for large-scale applications due to the compelling advantages of the cathode material sulfur, *viz.* its natural abundance, environmentally friendly nature, and high theoretical capacity (1675 mAh g^{-1}) [1,2]. However, during the operation of a Li–S cell, the sulfur cathode undergoes a sluggish redox reaction process accompanied by multiphase transformation involving insoluble S_8, soluble lithium polysulfides (LiPSs) and insoluble Li_2S_2/Li_2S [3]. This results in incomplete sulfur transformation, causing soluble LiPSs to accumulate in the electrolyte, which exacerbates the shuttle effect, leading to a low specific capacity of the cathode and a fast capacity fade [4–6]. Much effort has been dedicated to developing efficient electrocatalysts in the form of nanoparticles or as monodisperse single metal atoms (SACs) loaded on carbon substrates with the aim of promoting the kinetics of the redox reaction taking place at the sulfur cathode [7–10]. Electrocatalysts including metals, metal oxides, metal sulfides, and metal nitrides have been found to catalyze the transformation of sulfur species.

The main challenge in developing electrocatalysts for Li–S batteries lies in promoting the complex sulfur conversion reaction. The sulfur redox reaction (SRR) is a cascade reaction starting with reactant S_8, followed by complex intermediates Li_2S_x (x = 2, 4, 6, 8) to finally form Li_2S. An effective catalyst can successfully provide active sites for the consecutive activation of a series of intermediates with complex molecular structures [11–14]. Hence, to accelerate the catalytic transformation, we need to design active binding sites that optimally balance the requirements of all steps in the catalytic cycle, especially at a low mass loading of the catalyst. SACs have a nearly 100% atom utilization efficiency, which allows a much lower mass loading than nanoparticles when used as a catalyst in Li–S batteries. However, the binding strength of polysulfides to a particular active metal site can be variable [15]. For example, the calculated binding energy of Li_2S_6 on V–N_4–C SAC is 3.37 eV, but it increases to 4.71 eV for Li_2S on the same metal active center [16]. The binding strength is also dependent on the type of SAC, e.g., the Fe–N_4–C SAC exhibits a weaker adsorption towards both Li_2S_6 (1.60 eV) and Li_2S (2.56 eV). Due to their relatively simple composition, conventional SACs provide little room for tuning the center metal atom-LiPSs interaction to optimize its interaction with different LiPSs [17–19]. In contrast to SACs with totally isolated monoatomic sites, dual-atom catalysts have an additional interaction, namely, a metal–metal interaction, that gives the possibility of inducing synergistic effects through orbital interactions to allow electron transfer between adjacent paired metal atoms. Previous reports have shown that the electronic properties of dual-atom catalysts (DACs) can be favorably exploited towards SRR [20–22]. These effects have been mainly ascribed to a synergistic effect between the two adjacent metal centers that modifies catalytic behavior, even though the atomistic details of this effect remain underexplored. This study was complicated by the multistep process in SRR, which requires *operando* structural analysis on electrocatalysts with precisely controlled structures.

Herein, we report a DAC consisting of Pt–Cu dual-atomic sites anchored on nitrogen-doped graphene (Pt/Cu-NG). Electrochemical measurements confirmed the superior catalytic activity of the Pt/Cu-NG catalytic system on the kinetics of sulfur redox reactions; the catalytic activity of our DAC system surpassed those of the SACs Pt-NG and Cu-NG, as well as a mixture of the two. The S@Pt/Cu-NG electrode (S mass ratio of 80 wt%) exhibited a much higher electrochemical performance in a pouch cell. *Operando* X-ray absorption spectroscopy (XAS) and density functional theory (DFT) calculations indicate that the excellent electrocatalytic activity of the Pt/Cu-NG system originates from a synergistic effect between atomic Pt–Cu dual sites. The interatomic orbital interaction and charge transfer within paired Pt and Cu atoms effectively modulate the electronic structure of Pt, resulting in an optimal moderate interaction of the metal atom to the Li–S species. Our findings therefore provide a comprehensive understanding of the atomic-level phenomena in dual-atom catalysis. More specifically, using a combination of *operando* experiments and theory, we elucidate the synergistic effects present in double-atom active sites and their crucial role in improving the kinetics of sulfur redox reactions. We believe that such a comprehensive holistic understanding will provide a much-needed boost to designing efficient electrocatalysts for advanced Li–S batteries and enable their wide application.

2. Material and methods

2.1. Synthesis of catalytic materials

Cu-NG was prepared by pyrolysis of mixtures containing metal salts and graphene oxide (GO) powder under an NH_3 atmosphere. Nitrogen-doped graphene (NG) was prepared by the same method except that no metal salt was added to the GO suspension. For more details, see Supplementary Text S1. The preparation of Pt/Cu-NG was carried out in a viscous atomic layer deposition (ALD) flow reactor (GEMSTAR-6 Benchtop ALD, Arradiance) using trimethyl(methylcyclopentadienyl)-platinum (IV) ($MeCpPtMe_3$, 99%) and ultrahigh purity O_2 (99.999%) as precursors with ultrahigh purity N_2 (UHP, 99.999%) as the carrier gas at a flow rate of 150 mL min^{-1}. The Pt precursor was heated to 65 °C to obtain a sufficiently high vapor pressure. The reactor inlets were held at 100 °C to avoid any precursor condensation. Pt was deposited on Cu-NG at 200 °C for one cycle. The timing sequence was 12, 180, 12, and 180 s for $MeCpPtMe_3$ exposure, N_2 purge, O_2 exposure, and N_2 purge, respectively. Pt was deposited on NG using the same ALD procedure to prepare Pt/NG.

2.2. Operando X-ray absorption spectroscopy measurements

Operando XAS experiments were carried out using a homemade electrochemical cell. XAFS data were recorded at room temperature in fluorescence mode using a Lytle detector. The measured X-ray absorption fine structure (XAFS) raw data were then background-subtracted, normalized and Fourier transformed in Athena. Extended XAFS (EXAFS) fitting was performed for the FT k^2-weighted experimental EXAFS signals using Artemis software. Cu K-edge theoretical X-ray absorption near-edge structure (XANES) calculations were carried out with finite difference method near edge structure (FDMNES) code in the framework of the real-space full multiple scattering (FMS) scheme using the muffin-tin approximation for the potential. With increasing temperature, the amplitude of the crystal lattice vibrations increases, leading to a broadening of the XANES spectra. We have taken into account the effect

of temperature during the XANES simulation and the spectra convoluted using a Gaussian function to account for the broadening.

3. Theory/calculation

First-principles calculations were performed based on *ab initio* DFT using the VASP 5.4.4 program. The generalized gradient approximation and Perdew–Burke–Ernzerhof exchange-correlation functional were adopted. A well-converged plane-wave cutoff of 500 eV was used and the atomic coordinates were allowed to relax until the forces on the ions were less than 0.03 eV $Å^{-1}$. The electronic convergence criterion was set to 1×10^{-5} eV. The reduced Brillouin zone was sampled with a Γ-centered $2 \times 2 \times 1$ k-point mesh for optimization and a $3 \times 3 \times 1$ k-point mesh for static calculations. A denser $9 \times 9 \times 1$ k-point mesh was used to calculate the density of states. A 20 Å vacuum space was used in all the calculations to avoid interactions between the periodic images. The models for single/dual-atom catalysts were constructed using a 7×7 supercell of graphene. Grimme D3 correction was used to describe the weak van der Waals interactions. The formation energies of Pt–Cu dual-atomic structures were calculated by the formula: $E_{form} = E_{DAC} - E_{sub\_Cu} - E_{Pt}$, where E_{DAC}, E_{sub_Cu}, E_{Pt} represent energies of the considered dual-atomic structures, the corresponding Cu-NG substrates without Pt atom, a Pt atom in its bulk crystal, respectively. We selected the configuration with the most stable adsorption patterns from a variety of initial adsorption configurations as the optimal adsorption configuration for each adsorption structure. When calculating the formation energy of SACs or DACs with different structures, we adjusted the local coordination environment of metal atoms, including the types and positions of coordinating atoms, to finely control the bond lengths and bond angles between metals and coordinating atoms, thereby obtaining the least energetic structure. The adsorption energies (E_{ads}) of S_8 and several polysulfides on different surfaces were calculated by the following equation: $E_{ads} = E_{total} - E_{sub} - E_{adsorbate}$, where E_{total}, E_{sub} and $E_{adsorbate}$ are energies of the adsorption configuration, the catalyst substrates, and isolated S_8 and polysulfides molecules, respectively. The crystal orbital Hamilton population (COHP) analysis was performed with the LOBSTER 4.1.0 package. The barriers for Li_2S decomposition on catalysts were calculated with the climbing-image nudged elastic band (CI-NEB) method to evaluate de-lithiation reaction kinetics.

3.1. Material characterization

High-angle annular dark-field scanning transmission electron microscopy (HADDF-STEM) images were obtained by a JEOL JEM-ARF200F TEM/STEM instrument with a spherical aberration corrector operated at 200 kV and 80 kV. Thermogravimetric analysis (TGA) was carried out using a TA Q5000IR TGA under a flowing N_2 atmosphere with a heating rate of 10 °C min^{-1}. X-ray photoelectron spectroscopy (XPS) was performed on a Thermo ESCALAB 250Xi instrument with Al Kα radiation (1484.6 eV) as the excitation source. Metal loading in the samples was determined by inductively coupled plasma-atomic emission spectroscopy (ICP–AES) using an Optima 7300 DV spectrometer. X-ray powder diffraction patterns were acquired on a Rigaku X-ray diffractometer using Cu-Kα radiation as the X-ray source.

3.2. Li–S cell assembly and electrochemical characterization

See Supplementary Text S2.

4. Results and discussion

To demonstrate the synergistic effect of DACs that can effectively promote the sulfur redox reaction. Thus, the Cu and Pt atoms with little catalyzing effect are selected. The procedure to create Pt–Cu diatomic sites on nitrogen-doped graphene (Pt/Cu-NG) is presented in Figs. S1−S6 and in the Experimental Section. The aberration-corrected high-angle annular dark-field scanning transmission electron microscopy (HADDF-STEM) images show that Pt–Cu bimetallic sites can be well recognized by their different contrast due to their large difference in atomic number (Figs. 1a and b). Isolated single-Cu atoms (Cu-NG) and Pt single atoms (Pt-NG) on nitrogen-doped graphene were also prepared as the control samples (Figs. S2, S4–S6). The chemical states of Pt and Cu atoms in Pt/Cu-NG were identified by XAS. The oxidation state of Pt atoms in Pt-NG is calculated to be approximately +2.34, whereas it is +2.07 in Pt/Cu-NG (Figs. S7 and S8). However, the mean oxidation state of Cu atoms in Cu-NG is calculated to be +1.59, which is lower than that in Pt/Cu-NG (+1.67) (Figs. S9 and S10). The opposite trend in the change in the oxidation state of the Cu and Pt atoms in Pt/Cu-NG in comparison with Cu-NG and Pt-NG strongly demonstrates electronic interactions between the Pt and Cu atoms in Pt/Cu-NG, which is further confirmed by XPS, Fig. S11 and differential charge density analyses (Fig. S12). The Cu and Pt loadings in Pt/Cu-NG were determined to be ~0.36 and ~0.78 wt%, respectively, by inductively coupled plasma-atomic emission spectroscopy (ICP–AES). This corresponds to a Cu/Pt atomic ratio of 1.4. Assuming that all Pt atoms are paired with copper atoms, there would still be 28.5% of Cu atoms remain unutilized. Increasing the cycle numbers of Pt ALD to enhance the content of Pt–Cu atomic pairs results in the observation of nanoparticles or clusters on the graphene sheets (Fig. S13).

Unveiling the local structures of these catalysts is critical to understanding their synthesis mechanism and their catalytic applications. Through XAS and DFT analysis, we successfully determined the most likely atomic configuration for Pt/Cu-NG, as depicted in Fig. 1c. The detailed process of structural analysis is outlined below. In our work, the Pt atoms in Pt/Cu-NG are introduced after the formation of Cu single sites. Therefore, we first investigated the local atomic coordination configuration of Cu-NG. The Fourier transform extended X-ray absorption fine structure (FT-EXAFS) spectra at the Cu K-edge are illustrated in Fig. S14. Cu-NG exhibits a main peak at 1.49 Å, which could be attributed to Cu–C/N coordination. Quantitative EXAFS curve fitting analysis gives a coordination number (CN) of four for Cu-NG, which we assign to Cu–C/N (Fig. S15a and Table S1). Considering the limit of EXAFS fitting in differentiating Cu–C and Cu–N coordination because of the close scattering amplitude of C and N, the coordination configurations of Cu may have seven types of structures by varying the number of C and N atoms, as shown in Fig. S16. To determine the most likely coordination structures of Cu atoms in Cu-NG, DFT calculations were performed based on the above proposed local coordination structures (Fig. S16). Five of them have a much lower formation energy of <-2.0 eV, demonstrating that these structures are energetically favorable. Next, we continued our path toward resolving the atomic-site structure in Cu-NG by comparing the simulated XANES spectra with the experimental spectra. The results show that all simulated spectra are drastically different from the experimental spectra except Cu–C_2N_2-1 (Fig. S17). All the features for the experimental spectra are correctly reproduced for the Cu–C_2N_2-1 structure, especially for the weak pre-edge peak a and WL peak b. Together, these XANES simulations provide the solid spectroscopic fingerprint that a single Cu metal center presents in the form of Cu–C_2N_2-1 in the first coordination sphere, which is fully consistent with the EXAFS results.

After we confirmed the structure of Cu-NG, we investigated the EXAFS-wavelet transform (EXAFS-WT) spectra of Pt/Cu-NG at the Cu K-edge to determine that the coordination structure of Cu is uncharged after introducing Pt atoms into Cu-NG. EXAFS-WT analyses of Cu-NG and Pt/Cu-NG show an identical intensity maximum at 4.2 $Å^{-1}$ (Fig. S18). The EXAFS fitting results further show that the coordination number of Cu–C/N paths in Pt/Cu-NG is estimated to be 4, confirming that the first coordination shell of Cu atoms is similar to that of Cu-NG (Fig. S15b and Table S1). Once we have determined the coordination configuration of the Cu atom in Pt/Cu-NG, the EXAFS spectrum of Pt/Cu-NG at the Pt L_3-edge is obtained to identify the local structure of the Pt atom. In the FT-EXAFS at the Pt L_3 edge (Fig. S19), one prominent peak at 1.55 Å assigned to Pt–C/N coordination is observed for Pt/Cu-NG. The coordination

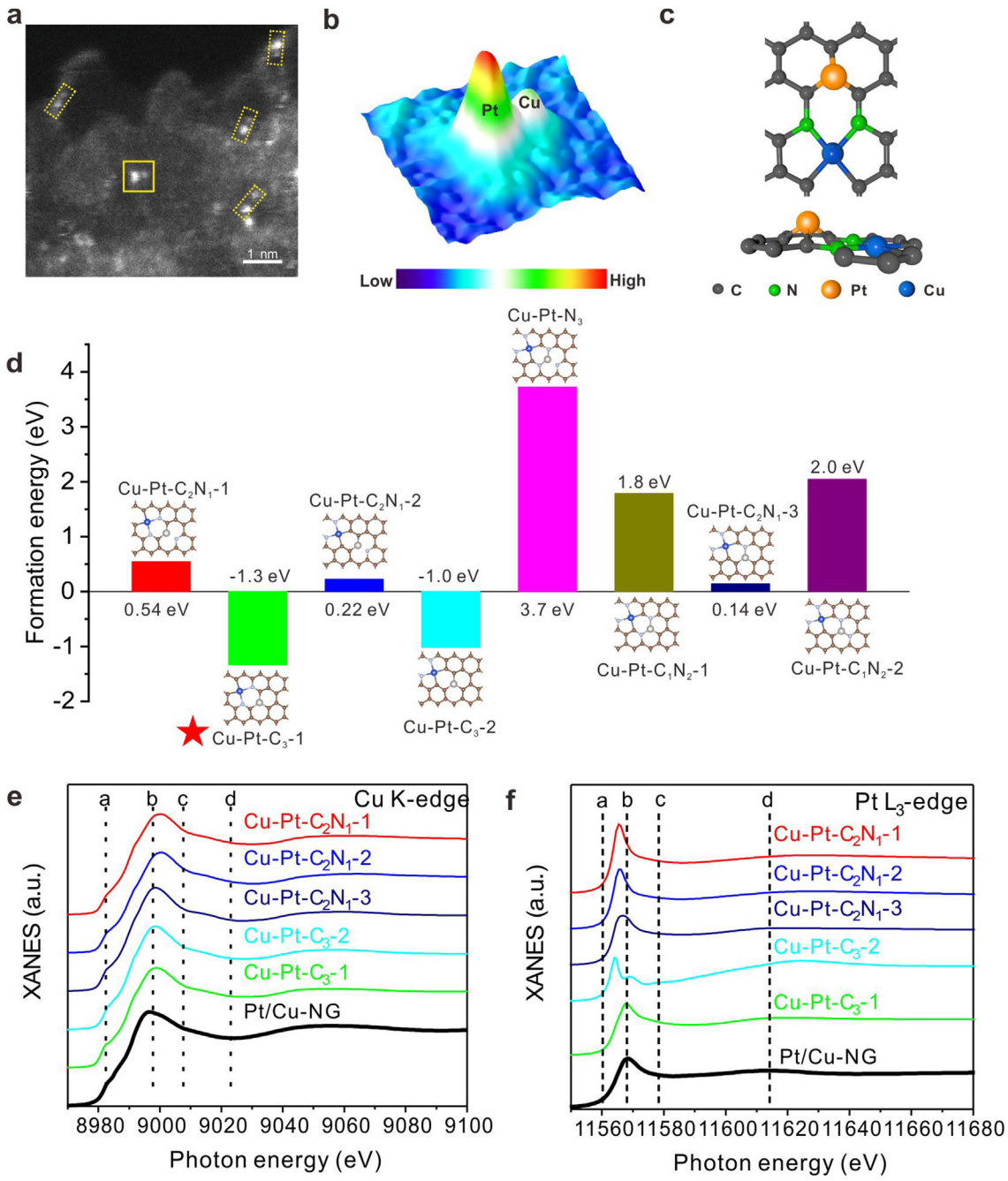

Fig. 1. Synthesis and structural characterization of Pt–Cu diatomic sites. (a) Aberration-corrected HAADF-STEM image of Pt/Cu-NG. (b) 3D atom-overlapping Gaussian-function fitting mappings of the area marked by the yellow square. (c) The most likely atomic configuration for Pt/Cu-NG. (d) The formation energy of Pt–Cu dual-atomic structures when Pt atoms are deposited on different substrates. The silver, blue, brown and light blue balls represent Pt, Cu, C and N atoms, respectively. (e) Comparison of the experimental Cu K-edge XANES spectrum of Pt/Cu-NG to the theoretical XANES spectrum. (f) Comparison of the experimental Pt L_3-edge XANES spectrum of Pt/Cu-NG to the theoretical XANES spectrum.

configurations for Pt/Cu-NG were then investigated by EXAFS curve-fitting analysis (Fig. S20). It is well fitted with a coordination number of Pt–C/N equal to three (Fig. S20b and Table S1). Therefore, we constructed a series of possible local coordination structures for the Pt–Cu diatomic site in the diatomic catalyst. In this case, the Cu atom is present in the coordinated form of Cu–C_2N_2-1, while the Pt atom is embedded in the graphene vacancy adjacent to the Cu site in the coordinated form of Pt-C_xN_{3-x}. DFT predictions are performed based on the above proposed local coordination structures with changes in carbon or nitrogen (Fig. 1d). The formation energy is the lowest for the Pt–Cu dual-atomic structure when Pt atoms are inlaid in the graphene vacancy adjacent to the Cu sites via three C atoms, indicating that this structure is energetically the most favorable. To demonstrate the soundness of our proposed Pt–Cu atomic configuration, we perform structural refinement based on the five kinds of Pt–Cu dual-atomic structures that have relatively low formation energy as determined by DFT by simulating Cu K-edge and Pt L_3-edge XANES spectra. As shown in Figs. 1e and f, all the features from "a" to "d" in the experimental Cu K-edge and Pt L_3-edge XANES spectra of Pt/Cu-NG can be correctly reproduced, which also convincingly validates the proposed structural model. We also followed a three-step approach similar to that used for determining the structure of Cu-NG, and the results demonstrate that Pt–C_2N_2-3 with N atoms at the crossing position is

the most likely structure for Pt-NG (Figs. S19−S22). To further investigate the stability of the three catalysts, we performed *ab initio* molecular dynamics (AIMD) simulations (Fig. S23). The AIMS simulations were performed for 5 ps with a time step of 1 fs with the NVT ensemble using the Nosé–Hoover thermostat at 1100 K, 500 K, and 500 K for Cu-NG, Pt-NG, and Pt/Cu-NG, respectively, according to their preparation temperature. The structures remained intact without damage and bond breakage, which proved the thermodynamic stability of the three selected structures and concluded that the catalyst structures were reasonably optimized. In summary, the combination of EXAFS fitting, DFT calculation and simulated XANES results unambiguously revealed the local structure of Cu-NG, Pt-NG and Pt/Cu-NG.

Catalysts are expected to enhance the conversion process of sulfur species in Li–S batteries. To pinpoint the dynamic changes in the electronic state and local coordination environment of Pt and Cu atoms during this typical multistep reaction and their impact on catalytic performance, *operando* XAS was performed. The working Li–S cell was discharged to 1.7 V and charged back to 2.7 V. For the Pt L_3-edge XANES (Figs. 2a and b), the WL intensity continues to decrease from OCV to 1.7 V and increases in the voltage range from 1.7 V to 2.7 V, pointing to a decrease in the number of unoccupied states of the Pt 5d orbital during discharge and an increase during charging. We note here that the WL intensity of the Cu K-edge XANES follows the same trend (Figs. 2c and d). This implies that the change in the electronic state of Cu atoms is reversible; this is also evidenced from the reversible shift of the absorption edge. These trends show that during the discharge/charge processes, charge transfer occurs in a reciprocal manner between the sulfur species and Pt/Cu atoms, leading to a reversible change in oxidation states. For a clearer comparison, we quantitively estimated the average oxidation state of Pt and Cu atoms at different states based on the fitted XANES curves (Figs. S7−S10). Under OCV conditions, the oxidation state of Pt atoms increases to +3.65 compared to pristine Pt/Cu-NG, while that of Cu atoms decreases to +1.57, pointing to the effective adsorption of S_8 molecules over the Pt–Cu dual-atom sites (Fig. 2e). Thus, when interacting with S_8 molecules, the oxidation states of Pt and Cu atoms change in the opposite direction with respect to their pristine counterpart, which in turn is related to their different catalytic behavior. In the subsequent discharge process, the oxidation states of both Pt and Cu atoms decrease and nearly return to their initial states. The highly reversible electronic structure of Pt–Cu diatomic sites is the key to enhancing the catalytic activity for Li–S redox reactions. Notably, the Pt atoms undergo a more dramatic change in oxidation state during the cycling process than the Cu atoms, which we attribute to the stronger interaction of Pt with the sulfur species. It is thus the Pt atom rather than the Cu atom that is preferentially adsorbed and enables the conversion of sulfur species on the Pt–Cu diatomic site. The introduction of Cu offers the possibility to indirectly modulate the electronic structure of Pt to significantly increase the binding energies of the sulfur species and thereby enhance charge transfer between Pt and S.

To probe the local structural evolution of the Pt–Cu dual-atom active sites occurring in situ, we performed *operando* FT-EXAFS at both Pt L_3- and Cu K-edges. In the FT-EXAFS spectra at the Pt L_3-edge (Fig. 2f), in

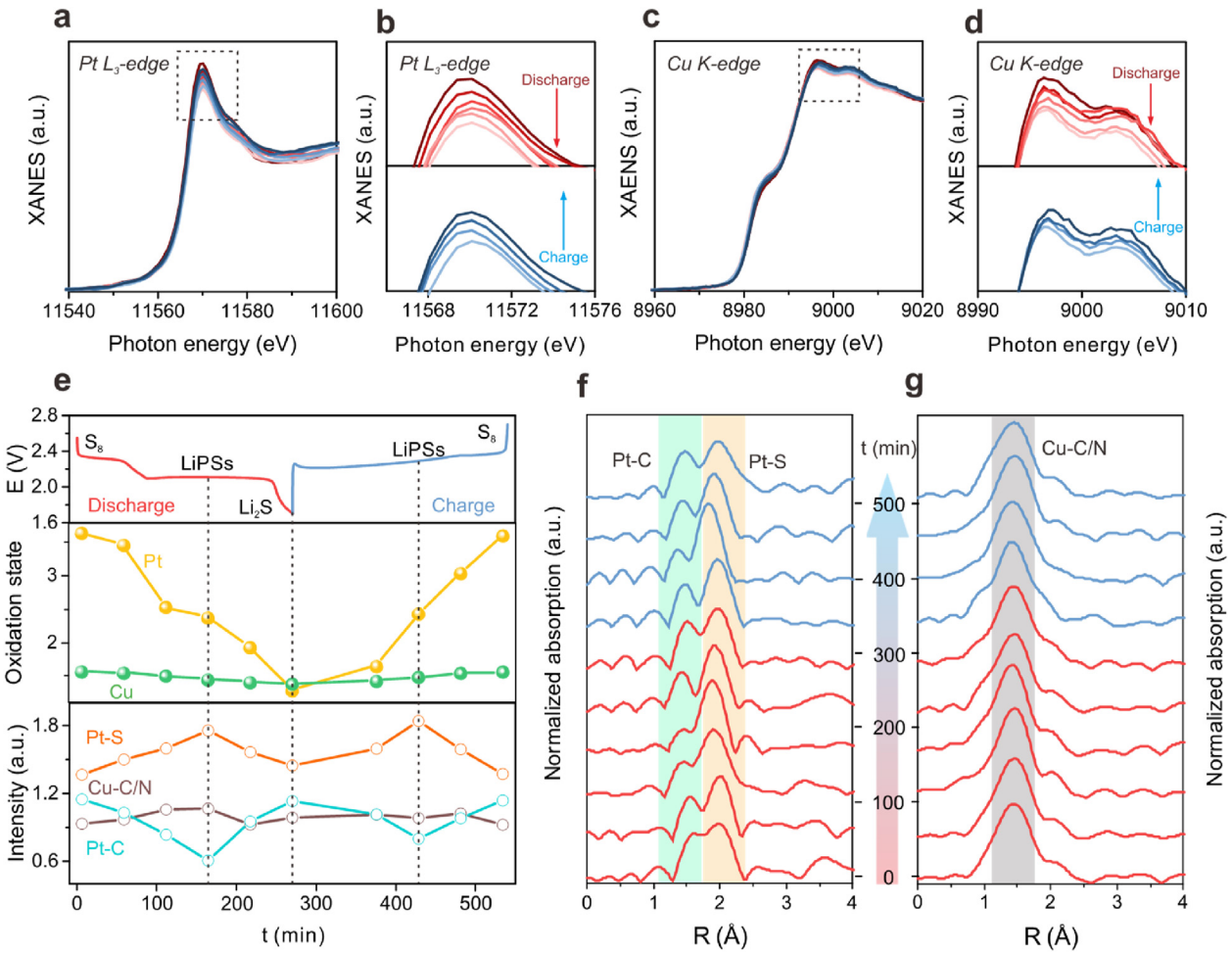

Fig. 2. *Operando* XAS characterization of Pt–Cu diatomic sites. *Operando* XANES spectra at the (a) Pt L_3-edge and (c) Cu K-edge recorded for the whole Li–S electrochemical reaction process. (b) and (d) are the magnified white-line peaks of the XANES region. (e) Evolution of the electronic states and local coordination environment of Pt/Cu atoms during electrochemical cycling. Corresponding FT-EXAFS spectra at the (f) Pt L_3-edge and (g) Cu K-edge.

addition to the original Pt–C/N coordination at 1.60 Å, a new peak appeared at approximately 1.98 Å when interacting with S_8 molecules at OCV, which remained present during the entire electrochemical reaction. XAS data from the literature indicate that this new signal from the Pt L_3-edge could arise from Pt–S bonds [23,24]. In contrast, the FT-EXAFS spectra at the Cu K-edge only exhibit a single large peak derived from the Cu–C/N scattering path during the entire electrochemical cycling process (Fig. 2g). This difference strongly suggests that the Pt sites rather than the Cu sites preferentially interact with the sulfur species. We further monitored the variation in amplitude of the first coordination shell (below 2 Å) of Pt and Cu atoms to reveal changes in the local coordination environment around the Pt–Cu diatomic sites (Fig. 2e). During the discharge process, an obvious increase in the Pt–S coordination amplitude can be seen as S_8 molecules are reduced to long chain lithium polysulfides. This peak reaches its maximum amplitude when discharged to the middle of the second plateau. With further discharge to 1.7 V, the amplitude of the Pt–S peak significantly decreases, which we attribute to the reduced amount of polysulfides in the electrolyte due to their effective conversion to insoluble Li_2S_2/Li_2S. In the subsequent charging process, the intensity of the Pt–S peak increases with the appearance of polysulfides and returns to its original intensity at the end of the cycling process. Notably, the amplitude of the Pt–C/N coordination shows a totally opposite trend to the Pt–S coordination. This "trade-off" between the amplitudes of Pt–C/N and Pt–S peaks is testimony to the dynamic evolution of the Pt atomic sites due to their strong interaction with the sulfur species, in good agreement with the XANES results above. In stark contrast, the peak intensity corresponding to the Cu–C/N scattering path exhibits almost no change, pointing to the structural stability of the Cu atomic sites and their relatively weak interaction with the sulfur species. Taken together, the *operando* XAS results clearly demonstrate the presence of a synergistic effect in the Pt–Cu diatomic active sites. The more dynamic coordination structure of Pt atoms facilitates the adsorption of the sulfur species on the diatomic catalytic sites through a strong interaction. Simultaneously, Cu atoms, with a stable coordination structure, enable the effective desorption of the sulfur species off the diatomic catalytic sites by enabling effective charge distribution. Thus, the synergistic catalytic behavior of Pt and Cu atoms is the reason for the high catalytic efficiency of Pt–Cu diatomic sites, which greatly enhances the sulfur redox reaction kinetics. The electronic and geometric structures of central dopant atoms could be adjustable by tailoring the carbon atoms. This adjustment alters the absorption activity of reactants on metal atoms, thereby influencing their catalytic properties. Thus, the carbon atoms neighboring the dopant atoms may also significantly contribute to SRR. However, the C K-edge XAS spectra of Pt-NG, Cu-NG, and Pt/Cu-NG exhibit minimal differences, potentially due to the low proportion of carbon atoms that bind with metal atoms (Fig. S24).

We performed electrochemical studies on the Pt/Cu-NG and control samples, including Pt-NG, Cu-NG, and a mixture of Pt-NG and Cu-NG prepared by hand grinding Pt-NG and Cu-NG in a 1:1 mass ratio (Pt-NG/Cu-NG). We first performed rotating disk electrode (RDE) measurements in a three-electrode cell using lithium foil as the counter and reference electrodes and a glassy carbon electrode loaded with catalyst as the working electrode. The electrolyte was 4 mM S_8 dissolved in 1 M LiTFSI in a 1:1 (v/v) DOL/DME mixture. Fig. 3a shows the linear sweep voltammetry (LSV) curves, where the onset potential and half-wave potential for Pt/Cu-NG are 2.47 V and 2.21 V, respectively, which are higher than those of the Pt-NG/Cu-NG mixture (2.44 V and 2.11 V), Cu-NG (2.43 V and 2.09 V) and Pt-NG (2.39 V and 2.06 V), suggesting enhanced kinetics of sulfur reduction when using Pt–Cu diatomic catalysts on NG. In addition, Pt/Cu-NG shows a minimum Tafel slope of 88 mV dec^{-1} compared to the Pt-NG/Cu-NG mixture (98 mV dec^{-1}), Cu-NG (100 mV dec^{-1}) and Pt-NG (136 mV dec^{-1}), demonstrating the intrinsically higher electrocatalytic activity of Pt/Cu-NG (Fig. S25). We calculated the number of electrons transferred during S_8 reduction based on the Koutecky–Levich equation (Fig. S26). In contrast to the control samples, the Pt/Cu-NG catalyst shows a higher electron transfer number (Fig. S27), suggesting that the presence of Pt–Cu diatomic sites leads to a more complete sulfur reduction reaction [25,26]. Next, we assembled

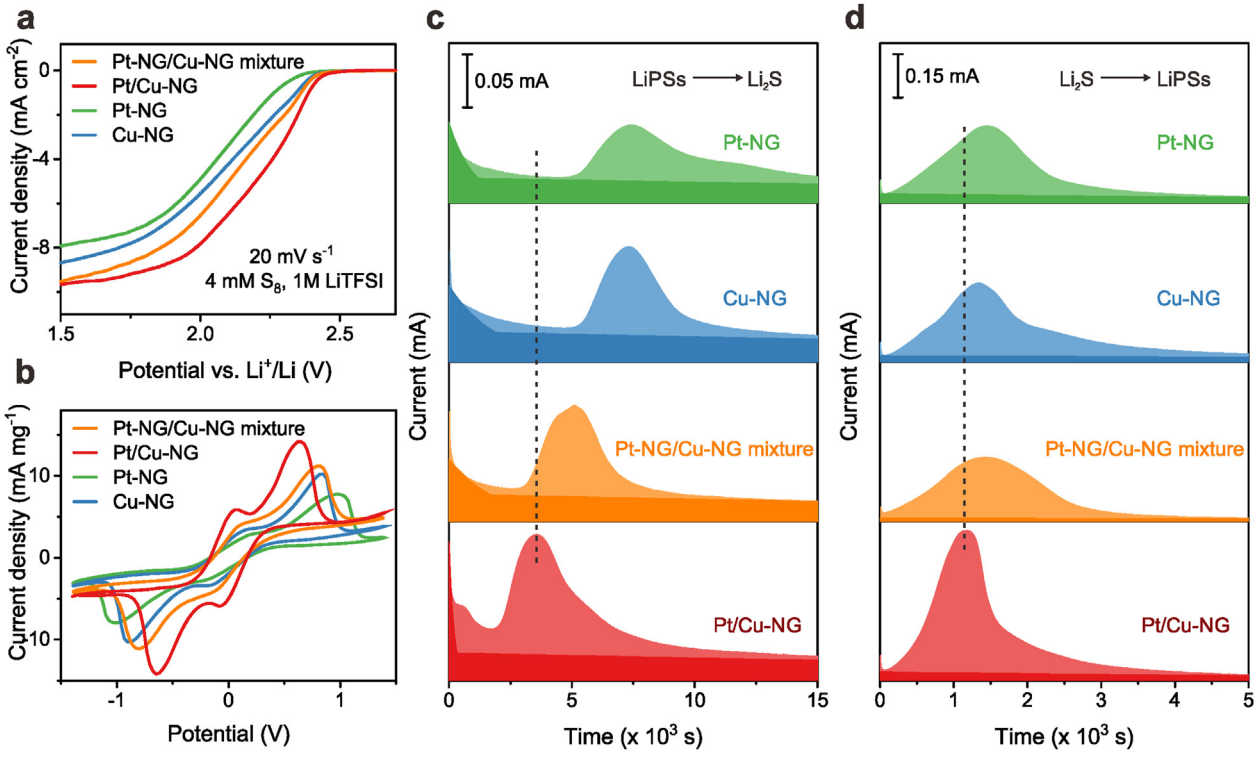

Fig. 3. Kinetic behavior of sulfur redox reactions. (a) LSV curves of Pt-NG, Cu-NG, the Pt-NG/Cu-NG mixture and Pt/Cu-NG towards the sulfur reduction reaction. (b) CV curves of Li_2S_6 symmetrical cells with the Pt-NG, Cu-NG, Pt-NG/Cu-NG mixture and Pt/Cu-NG electrodes. (c) Potentiostatic discharge profiles and (d) potentiostatic charge profiles of the Pt-NG, Cu-NG, Pt-NG/Cu-NG mixture and Pt/Cu-NG electrodes.

Li_2S_6 symmetric cells to further investigate the redox behavior of LiPSs on Pt-NG, Cu-NG, Pt-NG/Cu-NG mixtures and Pt/Cu-NG electrocatalysts. In all cases, the catalytic material was used as both the counter and the working electrode. Two pairs of reversible redox peaks are observed in all three cyclic voltammetry (CV) curves (Fig. 3b). Among the samples tested, Pt/Cu-NG exhibits the highest current response with distinct redox peaks, implying greater polysulfide conversion. Note that the CV profile of Pt/Cu-NG exhibits a much smaller separation between the reduction and oxidation peaks, demonstrating significantly improved reaction kinetics for polysulfide conversion [27]. The conversion of soluble LiPSs to Li_2S contributes to as much as 75% of the theoretical capacity, and due to its sluggish kinetics, it is the rate-determining step [28]. To investigate the advantages of Pt/Cu-NG in promoting Li_2S formation, we carried out potentiostatic discharge experiments using a Li_2S_8 catholyte as the active sulfur species. As shown in the potentiostatic nucleation profiles (Fig. 3c), Pt/Cu-NG exhibits a higher current intensity at a lower response time than the Pt-NG, Cu-NG and Pt-NG/Cu-NG mixtures, suggesting rapid LiPSs trapping and deposition of Li_2S on the Pt/Cu-NG electrode. Moreover, the capacity of Li_2S precipitation on Pt–Cu/NG (89 mAh g^{-1}) is higher than that of the Pt-NG/Cu-NG mixture (68 mAh g^{-1}), Cu-NG (65 mAh g^{-1}) and Pt-NG (56 mAh g^{-1}), confirming the enhanced kinetics of Li_2S deposition when using Pt–Cu/NG [29]. During charging, the sluggish oxidation kinetics of solid Li_2S are expected to hinder the reversibility of sulfur redox reactions. Therefore, we compared the reaction kinetics on the different catalytic materials by tracing the potentiostatic charge profiles to explore the oxidation behavior of Li_2S (Fig. 3d). Compared to the Pt-NG, Cu-NG and Pt-NG/Cu-NG mixtures, Pt/Cu-NG gave rise to a higher oxidation current peak in a shorter time, suggesting a significantly reduced energy barrier for Li_2S dissolution. Furthermore, the dissolution capacity of Li_2S estimated from the integral area under the potentiostatic charge curve was higher for Pt/Cu-NG than for the Pt-NG, Cu-NG and Pt-NG/Cu-NG mixtures, revealing effective oxidation of Li_2S on Pt/Cu-NG [30]. It is generally believed that carbon materials with a large specific surface area (SSA) could block LiPSs diffusion in the cathode region through physical adsorption. To determine the SSA of Pt-NG, Cu-NG, and Pt/Cu-NG, N_2 adsorption/desorption isotherms were obtained and are illustrated in Fig. S28. The SAA for Pt-NG, Cu-NG, and Pt/Cu-NG are measured at 101, 83, and 78 m^2 g^{-1}, respectively. To eliminate the influence of physical adsorption on catalytic behavior, an absorption test was conducted for Pt-NG, Cu-NG, and Pt/Cu-NG in a 3 mL 5 mM Li_2S_6 solution in DOL/DME. The optical image and UV–Visible spectrophotometry (UV–Vis) results are depicted in Fig. S29. All three solutions exhibited a nearly identical color, lighter than the blank Li_2S_6 solution. Furthermore, the UV–Vis curves for the three samples were analogous, indicating that LiPSs absorption is similar on Pt-NG, Cu-NG, and Pt/Cu-NG. Consequently, the SSA in Pt-NG, Cu-NG, and Pt/Cu-NG does not significantly impact catalytic activity performance. Taken together, these results point to the excellent electrocatalytic activity of Pt/Cu-NG in regulating the kinetics of sulfur redox reactions. The results from control experiments confirm that the Pt–Cu diatomic sites are responsible for the superior electrocatalytic activity of Pt/Cu-NG due to the synergistic effect between the Pt/Cu atoms.

To further understand the synergistic effect in the Pt–Cu diatomic active sites revealed by *operando* XAS results, we investigated the geometry and electronic structures of the metal active centers by DFT calculations (Figs. 4a–f). We used soluble Li_2S_4 as the representative sulfur species adsorbed on the metal active center for the following reasons: i) the electrochemical reaction of Li_2S_4 transfers 1/3 of the total charge involved in the conversion reaction of the cathode, and ii) the binding strength of Li_2S_4 is reported to be linearly correlated to the SRR overpotential [31]. We observed significant charge transfer between the Pt–Cu diatomic site and the Li_2S_4 molecule with the charge accumulation/depletion region centered near the Pt atom (Fig. 4c and Table S2), which induced a massive change in the Pt charge number (0.48 e^-) of the Pt–Cu site. This value is much higher than that of Cu (0.12 e^-) in the Pt–Cu diatomic site and those of Pt (0.17 e^-) and Cu (0.05 e^-) in the SACs (Figs. 4a and b and Table S2), implying a strongly covalent bonding Pt–S bond [32]. The strengths of the Pt–S, Cu–S, and S–S bonds were further analyzed by calculating the crystal orbital Hamilton population (COHP) and the integrated COHP (ICOHP) (Figs. 4d–f, S30 and S31). The Pt atom of Pt-NG and the Cu atom of Cu-NG bond to only the terminal S atom (S1) of Li_2S_4, forming Pt–S1 and Cu–S1, respectively, with ICOHP values of −3.72 and −0.13 (Figs. 4d and e). For Pt/Cu-NG, the Pt atom bonds to three S atoms, which are marked as Pt–S1, Pt–S2, and Pt–S3 with ICOHP values of −3.45, −3.85, and −3.22, respectively, which are more negative than that of Cu–S3 (−0.40) (Fig. 4f).

The more negative ICOHP values of Pt–S than Cu–S and the increased Pt–S bond number in Pt/Cu-NG together indicate that the S species preferentially interact with the Pt atom, and this tendency is reinforced when a Cu atom is sitting next to Pt and S. Thus, the binding energies of the sulfur species (e.g., S_8, Li_2S_4, and Li_2S) are increased (Figs. S32 and S33) with an enhanced degree of charge transfer between Pt and S (Fig. 4c). Considering the crucial role of solvation effects in modulating molecular structures and reaction behaviors in solutions, we incorporated an explicit solvation model (Fig. S34), which was compared to a vacuum model. Specifically, we allowed one or two 1,2-dimethoxyethane (DME) molecules to interact with S_8, Li_2S_4, and Li_2S [33]. We found that the solvent effects on the configurations of the three catalysts and their DFT energy calculations were very small after considering solvation, and the trend of the magnitude of the adsorption energies remained unchanged (Fig. S35). These results are in very good accordance with the synergy effect as indicated by *operando* XAS analysis.

In the Pt–Cu diatomic site, the strong Pt–S bonding assisted by Cu leads to a much weaker S–S bond in Li_2S_4, as indicated by the COHP analysis (Figs. 4d–f). When Li_2S_4 is attached to the Pt–Cu diatomic site, we observed a considerably greater occupation of the antibonding states for S–S than when Li_2S_4 is attached to the Pt and Cu single metal atom sites (Fig. S31). In particular, the bonding states of S2–S3 of Li_2S_4 on the Pt–Cu diatomic site are almost empty (or disappear, Fig. S31c). In comparison with Cu-NG and Pt-NG, the ICOHP values show a positive shift for Pt/Cu-NG, indicating weaker S–S binding when Li_2S_4 is adsorbed on the Pt–Cu diatomic site (Figs. 4d–f). The weaker S–S bond facilitates the reversible cleavage and recombination of polysulfides with faster reaction kinetics during electrochemical reduction/oxidation reactions in the cathode of the Li–S battery. Furthermore, we evaluated the Li_2S oxidation kinetics on different active sites by theoretical calculations (Fig. S36). The decomposition energy barrier of Li_2S was significantly decreased for the Pt–Cu diatomic site (0.64 eV) in contrast to that of the single Pt site (1.7 eV) and the Cu site (1.3 eV). The difference in the kinetics further proved the superiority of the Pt–Cu diatomic site. Single-atom catalysts containing Pt and Cu are found to be less active in catalyzing the sulfur redox reaction [34–36], which are more effective in demonstrating the effect of d-orbital electron coupling. The above synergistic effect in the Pt–Cu diatomic active sites unraveled by both *operando* XAS analysis (Fig. 2) and DFT calculations (Figs. 4a–f) can be briefly summarized as follows. The presence of Cu adjacent to the Pt atom facilitates the formation of a Pt–S bond and enables charge transfer between the di-metal atom active site and sulfur species, which weakens the S–S bond and thereby accelerates sulfur redox reaction kinetics (Fig. 4g). This synergy originates essentially from the interaction between the d orbitals of Cu and Pt atoms, raising the d bond center of Pt atoms close to the Fermi energy level, accompanied by a charge transfer from Cu to Pt atoms. The presence of highly populated and nearly continuous occupied and unoccupied states near the Fermi level (−0.095 eV) of Pt in Pt/Cu-NG (Figs. 4h and S37) is favorable for accepting/donating electrons from/to the sulfur species (Fig. 4i).

In view of the superior electrocatalytic activity of Pt–Cu dual sites towards SRR, we applied the S@Pt-NG, S@Cu-NG and S@Pt/Cu-NG composites as cathodes in Li–S full cells. The sulfur content was measured to be ~80 wt% (Fig. S38). Fig. 5a shows the galvanostatic discharge/charge profiles of the electrodes with an S mass loading of

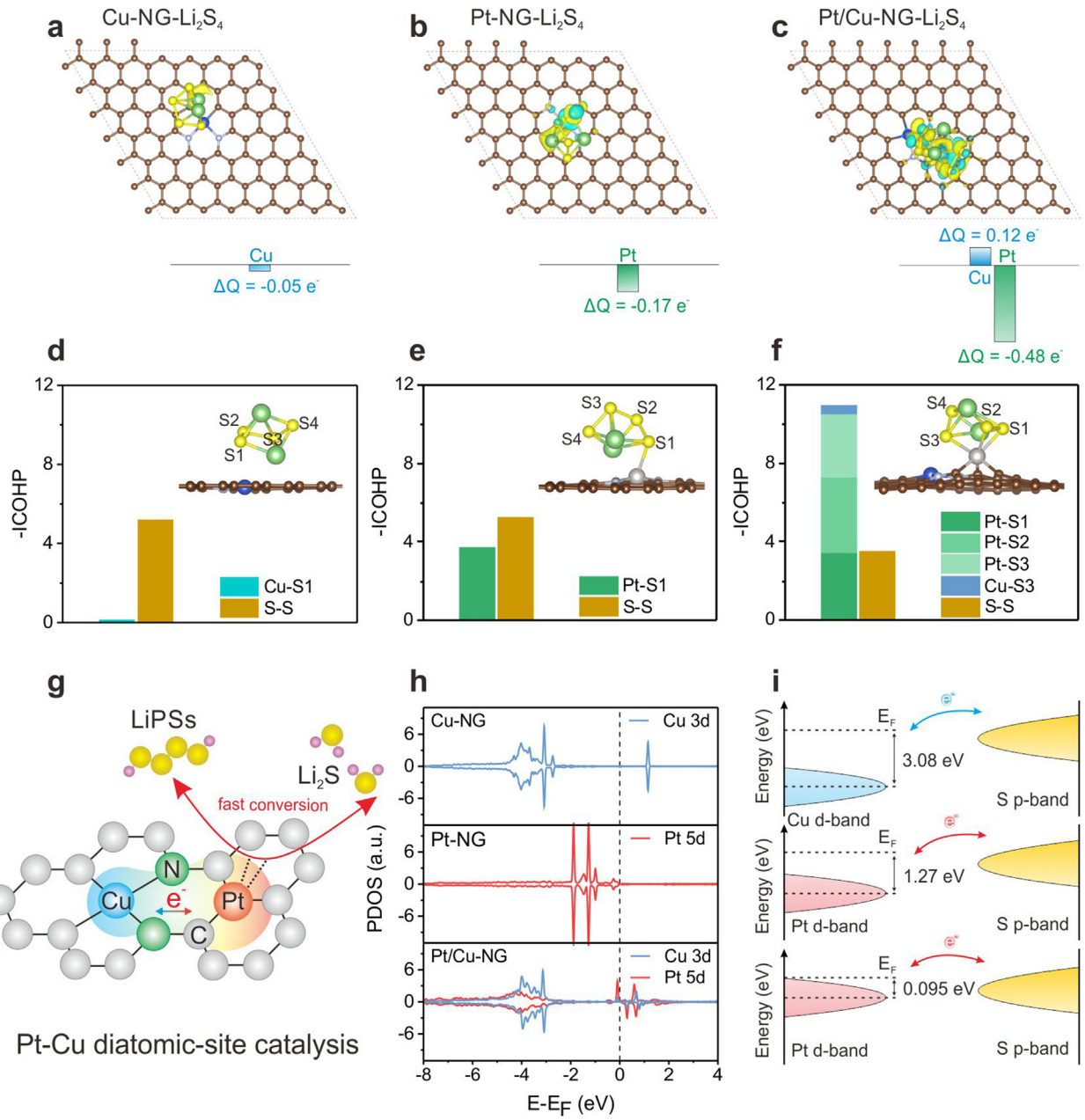

Fig. 4. DFT calculations on the catalytic processes. Differential charge density distribution of Li_2S_4 adsorbed on (a) Cu-NG, (b) Pt-NG, and (c) Pt/Cu-NG (yellow and cyan stand for charge accumulation and depletion). The isosurface is 0.003 e/bohr^3. Column charts in the lower panels represent the charge transfer number of Pt and Cu atoms upon Li_2S_4 adsorption. Crystal orbital Hamilton population (COHP) analysis of metal–S bonds and S–S bonds for Li_2S_4 adsorbed on (d) Cu-NG, (e) Pt-NG and (f) Pt/Cu-NG. Insets are configuration models for the Li_2S_4 adsorption system. (g) Schematic illustration of the proposed synergistic effect of Pt–Cu diatomic sites. (h) Projected density of states (PDOS) of metal atoms in Cu-NG, Pt-NG, and Pt/Cu-NG. (i) Schematic illustration of the *d*–*p* orbital hybridized density of states.

1.5 mg cm^{-2}. The S@Pt/Cu-NG electrode delivers an initial discharge capacity of 1185 mAh g^{-1} at 0.2 C, which is higher than that for S@Pt-NG (970 mAh g^{-1}) and S@Cu-NG (1033 mAh g^{-1}). At higher rates of 0.5 C, 1 C, 2 C and 4 C, the S@Pt/Cu-NG electrode shows satisfactory performance, with capacities of 976 mAh g^{-1}, 891 mAh g^{-1}, 810 mAh g^{-1} and 667 mAh g^{-1}, respectively (Fig. 5b). These values are considerably higher than those observed for the control samples, indicating the improved rate capability of S@Pt/Cu-NG. Furthermore, the acceleration of SRR promotes the transformation of dissolved LiPSs and thereby suppresses the shuttle effect, leading to improved cycling stability. The S@Pt/Cu-NG electrode exhibits a higher capacity retention rate of 83% after 100 cycles at 0.2 C (Fig. S39), compared to the S@Pt-NG (72%) and S@Cu-NG electrodes (74%). Long-term cycling stability tests were further carried out at 1 C, as shown in Fig. 5c. The S@Pt/Cu-NG electrode delivers a specific capacity of 680 mAh g^{-1} after 500 cycles with a capacity decay of 0.053% per cycle and a Coulombic efficiency of 99.5%. To assess the stability of Pt/Cu-NG, we conducted HAADF-STEM to confirm the dispersed state of Pt–Cu dual-atomic sites after 500 discharge–charge cycles under 1 C. The HAADF-STEM image (Fig. S40) illustrates that the Pt/Cu-NG species remain uniformly dispersed, with no discernible metal-related nanoparticles. This observation underscores the long-term stability of Pt/Cu-NG. In contrast, the specific capacity of the S@Pt-NG and S@Cu-NG electrodes declined progressively to only 345 mAh g^{-1} (capacity degradation rate of 0.10% and Coulombic efficiency of 97.9%) and 442 mAh g^{-1} (capacity degradation rate of 0.091% and Coulombic efficiency of 98.7%),

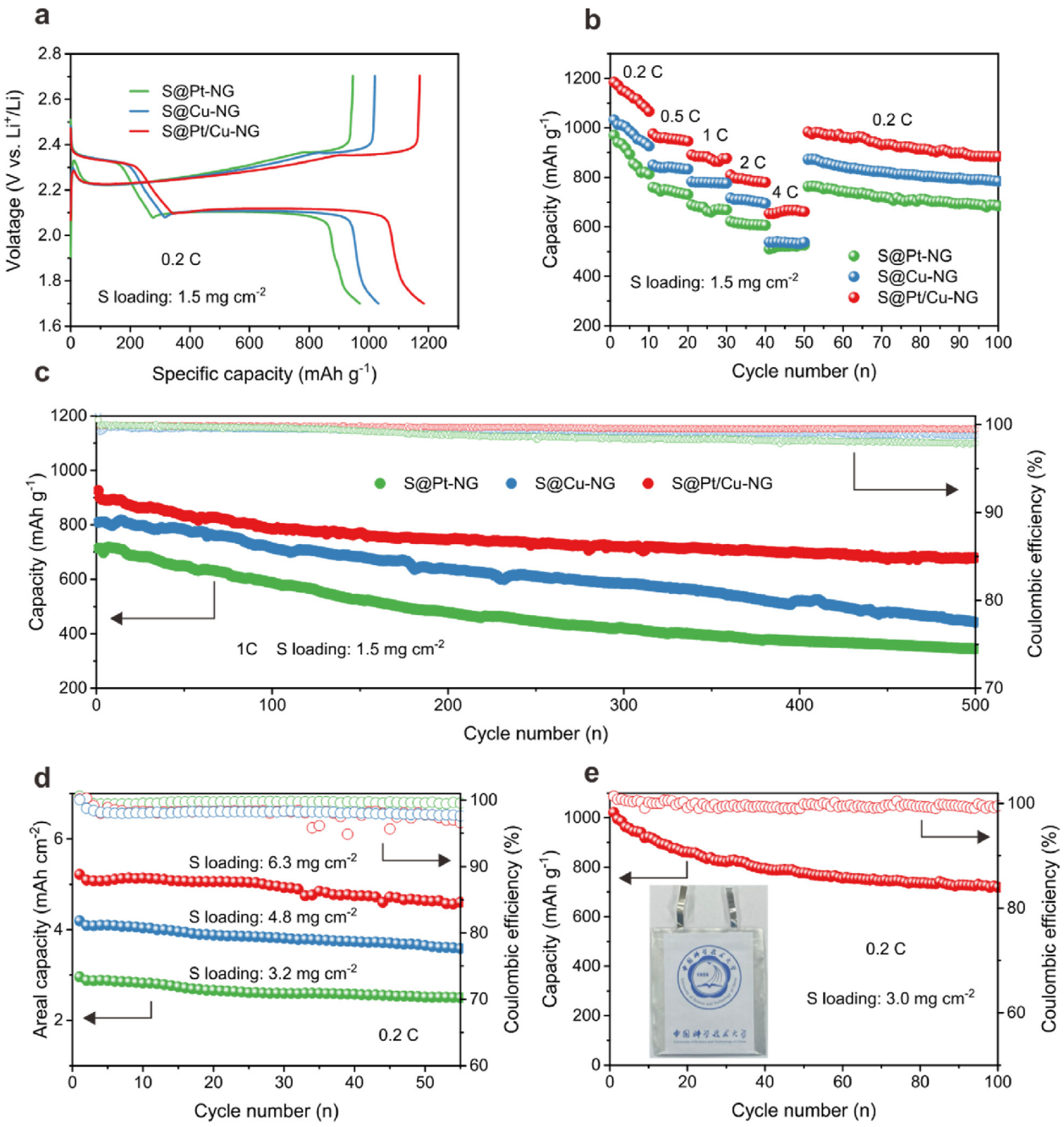

Fig. 5. Electrochemical performance of Li–S cells based on different cathodes. (a) Galvanostatic discharge/charge profiles of cells with the S@Pt/Cu-NG cathode at 0.2 C. (b) Rate capability of S@Pt-NG, S@Cu-NG and S@Pt/Cu-NG cathodes from 0.2 C to 4 C. (c) Long-term cycling performance and Coulombic efficiencies of the cells with S@Pt-NG, S@Cu-NG and S@Pt/Cu-NG cathodes at 1 C. (d) Cycling performance of S@Pt/Cu-NG cathodes with high sulfur loading at 0.2 C. (e) Cycling performance of the Li–S pouch cell with Pt/Cu-NG as the cathode catalyst.

respectively. The cycling performances of the S@Pt/Cu-NG electrode with high sulfur loadings of 3.2, 4.8, and 6.3 mg cm^{-2} were evaluated (Fig. 5d). Notably, the electrodes with high sulfur loadings of 6.3 mg cm^{-2} still delivered an initial areal capacity of 5.2 mAh cm^{-2}. We also fabricated a Li–S pouch cell based on an S@Pt/Cu-NG cathode with a sulfur loading of 3.0 mg cm^{-2}, which delivered an initial discharge capacity of 1021 mAh g^{-1} corresponding to an areal capacity of 3.0 mAh cm^{-2} and a reversible capacity of 720 mAh g^{-1} after 100 cycles at 0.2 C (Figs. 5e and S41), demonstrating the suitability of Pt–Cu DACs at practical sulfur loadings used in a working battery. A "Pt–Cu"-shaped light-emitting diode (LED) array with 88 bulbs could be powered by the assembled pouch cell when folded or bent in different ways, showing the application potential of the S@Pt/Cu-NG electrode in flexible Li–S batteries (Fig. S41).

5. Conclusions

In summary, we successfully created atomically dispersed Pt–Cu diatomic active sites on nitrogen-doped graphene. The Pt–Cu diatomic sites were found to be highly efficient electrocatalysts for multiphase sulfur redox reactions, outperforming single-atom Cu and Pt sites. The combination of *operando* XAS analysis and DFT calculations revealed a synergistic effect in the Pt–Cu dual-atom catalytic sites, arising from the modulated density of states of the Pt atom by the adjacent Cu. This

facilitates the formation of the Pt–S bond and charge transfer between the di-metal atom active site and sulfur species. As a result, the S–S bond is weakened, resulting in accelerated sulfur redox reaction kinetics. When applied in working Li–S coin cells, the S@Pt/Cu-NG electrode enabled a stable long-term cycling performance with a small capacity fading of 0.053% per cycle after 500 cycles at 1 C and a high areal capacity of 5.2 mAh cm^{-2} at high sulfur loading (6.3 mg cm^{-2}) at 0.2 C, demonstrating great potential for practical application. Our findings therefore provide insight at the atomic level in dual-atom catalysis and shed light on synergistic effects present in double-atom active sites that play a crucial role in improving the kinetics of sulfur redox reactions.

Author contributions

Shuai Xie: Writing – original draft, Methodology, Data curation, Conceptualization. **Xingjia Chen:** Methodology, Data curation. **Leilei Wang:** Methodology, Data curation. **Guikai Zhang:** Data curation. **Haifeng Lv:** Methodology. **Guolei Cai:** Methodology. **Ying-Rui Lu:** Methodology. **Ting-Shan Chan:** Methodology. **Jing Zhang:** Methodology. **Juncai Dong:** Methodology. **Hongchang Jin:** Methodology. **Xianghua Kong:** Writing – review & editing. **Junling Lu:** Writing – review & editing, Methodology. **Song Jin:** Writing – review & editing, Data curation, Conceptualization. **Xiaojun Wu:** Writing – review & editing, Supervision, Methodology, Data curation. **Hengxing Ji:** Writing – review & editing, Supervision, Project administration, Funding acquisition, Conceptualization.

Declaration of competing interest

The authors declare no competing financial interests.

Acknowledgments

This work was supported by the Natural Science Foundation of China (22125902, 21975243, U2032202, and U1932201), the National Program for Support of Topnotch Young Professionals, the DNL Cooperation Fund, CAS (DNL202020), the Anhui Science Fund for Distinguished Young Scholars (2208085J15), the National Key R&D Program of China (2022YFA1504101) and Users with Excellence Program of Hefei Science Center CAS (2021HSC-UE002).

Appendix A. Supplementary data

Supplementary data to this article can be found online at https://doi.org/10.1016/j.esci.2023.100222.

References

[1] Y. Li, S. Guo, Material design and structure optimization for rechargeable lithium-sulfur batteries, Matter 4 (2021) 1142–1188.
[2] Y. Chen, T. Wang, H. Tian, D. Su, Q. Zhang, G. Wang, Advances in lithium-sulfur batteries: from academic research to commercial viability, Adv. Mater. 33 (2021) 2003666.
[3] S.-F. Ng, M.Y.L. Lau, W.-J. Ong, Lithium-sulfur battery cathode design: tailoring metal-based nanostructures for robust polysulfide adsorption and catalytic conversion, Adv. Mater. 33 (2021) 2008654.
[4] J. Liang, Z.-H. Sun, F. Li, H.-M. Cheng, Carbon materials for Li-S batteries: functional evolution and performance improvement, Energy Stor. Mater. 2 (2016) 76–106.
[5] Z.W. Seh, Y. Sun, Q. Zhang, Y. Cui, Designing high-energy lithium-sulfur batteries, Chem. Soc. Rev. 45 (2016) 5605–5634.
[6] Y.V. Mikhaylik, J.R. Akridge, Polysulfide shuttle study in the Li/S battery system, J. Electrochem. Soc. 151 (2004) A1969.
[7] H. Ye, J.Y. Lee, Solid additives for improving the performance of sulfur cathodes in lithium-sulfur batteries-adsorbents, mediators, and catalysts, Small Methods 4 (2020) 1900864.
[8] P. Wang, B. Xi, M. Huang, W. Chen, J. Feng, S. Xiong, Emerging catalysts to promote kinetics of lithium-sulfur batteries, Adv. Energy Mater. 11 (2021) 2002893.
[9] Z. Liang, J. Shen, X. Xu, F. Li, J. Liu, B. Yuan, Y. Yu, M. Zhu, Advances in the development of single-atom catalysts for high-energy-density lithium-sulfur batteries, Adv. Mater. 34 (2022) 2200102.
[10] F. Wang, J. Li, J. Zhao, Y. Yang, C. Su, Y.L. Zhong, Q.-H. Yang, J. Lu, Single-atom electrocatalysts for lithium sulfur batteries: progress, opportunities, and challenges, ACS Mater. Lett. 2 (2020) 1450–1463.
[11] M. Vijayakumar, N. Govind, E. Walter, S.D. Burton, A. Shukla, A. Devaraj, J. Xiao, J. Liu, C. Wang, A. Karim, S. Thevuthasan, Molecular structure and stability of dissolved lithium polysulfide species, Phys. Phys. Chem. Chem. Phys. 16 (2014) 10923–10932.
[12] T. Zhang, L. Zhang, Y. Hou, MXenes: synthesis strategies and lithium-sulfur battery applications, eScience 2 (2022) 164–182.
[13] Z. Shen, X. Jin, J. Tian, M. Li, Y. Yuan, S. Zhang, S. Fang, X. Fan, W. Xu, H. Lu, J. Lu, H. Zhang, Cation-doped ZnS catalysts for polysulfide conversion in lithium-sulfur batteries, Nat. Catal. 5 (2022) 555–563.
[14] S. Xie, X. Chen, C. Wang, Y.-R. Lu, T.-S. Chan, C.-H. Chuang, J. Zhang, W. Yan, S. Jin, H. Jin, X. Wu, H. Ji, Role of the metal atom in a carbon-based single-atom electrocatalyst for Li-S redox reactions, Small 18 (2022) 2200395.
[15] Q.-W. Zeng, R.-M. Hu, Z.-B. Chen, J.-X. Shang, Single-atom Fe and N co-doped graphene for lithium-sulfur batteries: a density functional theory study, Mater. Res. Express 6 (2019) 095620.
[16] E.I. Andritsos, C. Lekakou, Q. Cai, Single-atom catalysts as promising cathode materials for lithium-sulfur batteries, J. Phys. Chem. C 125 (2021) 18108–18118.
[17] L. Ma, J. Qian, Y. Li, Y. Cheng, S. Wang, Z. Wang, C. Peng, K. Wu, J. Xu, I. Manke, C. Yang, P. Adelhelm, R. Chen, Binary metal single atom electrocatalysts with synergistic catalytic activity toward high-rate and high areal-capacity lithium-sulfur batteries, Adv. Funct. Mater. 32 (2022) 2208666.
[18] Y. Feng, L. Zu, S. Yang, L. Chen, K. Liao, S. Meng, C. Zhang, J. Yang, Ultrahigh-content Co-P cluster as a dual-atom-site electrocatalyst for accelerating polysulfides conversion in Li-S batteries, Adv. Funct. Mater. 32 (2022) 2207579.
[19] Z. Du, X. Chen, W. Hu, C. Chuang, S. Xie, A. Hu, W. Yan, X. Kong, X. Wu, H. Ji, L.-J. Wan, Cobalt in nitrogen-doped graphene as single-atom catalyst for high-sulfur content lithium-sulfur batteries, J. Am. Chem. Soc. 141 (2019) 3977–3985.
[20] L. Shen, Y.-W. Song, J. Wang, C.-X. Zhao, C.-X. Bi, S.-Y. Sun, X.-Q. Zhang, B.-Q. Li, Q. Zhang, Synergistic catalysis on dual-atom sites for high-performance lithium-sulfur batteries, Small Struct. 4 (2023) 2200205.
[21] X. Sun, Y. Qiu, B. Jiang, Z. Chen, C. Zhao, H. Zhou, L. Yang, L. Fan, Y. Zhang, N. Zhang, Isolated Fe-Co heteronuclear diatomic sites as efficient bifunctional catalysts for high-performance lithium-sulfur batteries, Nat. Commun. 14 (2023) 291.
[22] C. Dong, C. Zhou, M. Wu, Y. Yu, K. Yu, K. Yan, C. Shen, J. Gu, M. Yan, C. Sun, L. Mai, X. Xu, Boosting bi-directional redox of sulfur with dual metal single atom pairs in carbon spheres toward high-rate and long-cycling lithium-sulfur battery, Adv. Energy Mater. 13 (2023) 2301505.
[23] L. Wang, M.-X. Chen, Q.-Q. Yan, S.-L. Xu, S.-Q. Chu, P. Chen, Y. Lin, H.-W. Liang, A sulfur-tethering synthesis strategy toward high-loading atomically dispersed noble metal catalysts, Sci. Adv. 5 (2019) eaax6322.
[24] Q.-Q. Yan, D.-X. Wu, S.-Q. Chu, Z.-Q. Chen, Y. Lin, M.-X. Chen, J. Zhang, X.-J. Wu, H.-W. Liang, Reversing the charge transfer between platinum and sulfur-doped carbon support for electrocatalytic hydrogen evolution, Nat. Commun. 10 (2019) 4977.
[25] Y.-C. Lu, Q. He, H.A. Gasteiger, Probing the lithium-sulfur redox reactions: a rotating-ring disk electrode study, J. Phys. Chem. C 118 (2014) 5733–5741.
[26] L. Peng, Z. Wei, C. Wan, J. Li, Z. Chen, D. Zhu, D. Baumann, H. Liu, C.S. Allen, X. Xu, A.I. Kirkland, I. Shakir, Z. Almutairi, S. Tolbert, B. Dunn, Y. Huang, P. Sautet, X. Duan, A fundamental look at electrocatalytic sulfur reduction reaction, Nat. Catal. 3 (2020) 762–770.
[27] H. Lin, L. Yang, X. Jiang, G. Li, T. Zhang, Q. Yao, G.W. Zheng, J.Y. Lee, Electrocatalysis of polysulfide conversion by sulfur-deficient MoS_2 nanoflakes for lithium-sulfur batteries, Energy Environ. Sci. 10 (2017) 1476–1486.
[28] W.-G. Lim, S. Kim, C. Jo, J. Lee, Comprehensive review of materials with catalytic effects in Li-S batteries: enhanced redox kinetics, Angew. Chem. Int. Ed. 58 (2019) 18746–18757.
[29] F.Y. Fan, W.C. Carter, Y.-M. Chiang, Mechanism and kinetics of Li_2S precipitation in lithium-sulfur batteries, Adv. Mater. 27 (2015) 5203–5209.
[30] R. Wang, C. Luo, T. Wang, G. Zhou, Y. Deng, Y. He, Q. Zhang, F. Kang, W. Lv, Q.-H. Yang, Bidirectional catalysts for liquid-solid redox conversion in lithium-sulfur batteries, Adv. Mater. 32 (2020) 2000315.
[31] L. Wang, Z. Hu, X. Wan, W. Hua, H. Li, Q.-H. Yang, W. Wang, Li_2S_4 Anchoring governs the catalytic sulfur reduction on defective $SmMn_2O_5$ in lithium-sulfur battery, Adv. Energy Mater. 12 (2022) 2200340.
[32] S. Sun, X. Zhang, S. Wang, First-principles investigation on the bonding mechanism between graphyne and the (111) surface of Cu, Ag and Au, Mater. Res. Express 7 (2020) 065603.
[33] S. Feng, Z.-H. Fu, X. Chen, B.-Q. Li, H.-J. Peng, N. Yao, X. Shen, L. Yu, Y.-C. Gao, R. Zhang, Q. Zhang, An electrocatalytic model of the sulfur reduction reaction in lithium-sulfur batteries, Angew. Chem. Int. Ed. 61 (2022) e202211448.
[34] G. Zhou, S. Zhao, T. Wang, S.-Z. Yang, B. Johannessen, H. Chen, C. Liu, Y. Ye, Y. Wu, Y. Peng, C. Liu, S.P. Jiang, Q. Zhang, Y. Cui, Theoretical calculation guided design of single-atom catalysts toward fast kinetic and long-life Li-S batteries, Nano Lett. 20 (2020) 1252–1261.
[35] Z. Han, S. Zhao, J. Xiao, X. Zhong, J. Sheng, W. Lv, Q. Zhang, G. Zhou, H.-M. Cheng, Engineering d-p orbital hybridization in single-atom metal-embedded three-dimensional electrodes for Li-S batteries, Adv. Mater. 33 (2021) 2105947.
[36] Z. Zeng, W. Nong, Y. Li, C. Wang, Universal-descriptors-guided design of single atom catalysts toward oxidation of Li_2S in lithium-sulfur batteries, Adv. Sci. 8 (2021) 2102809.